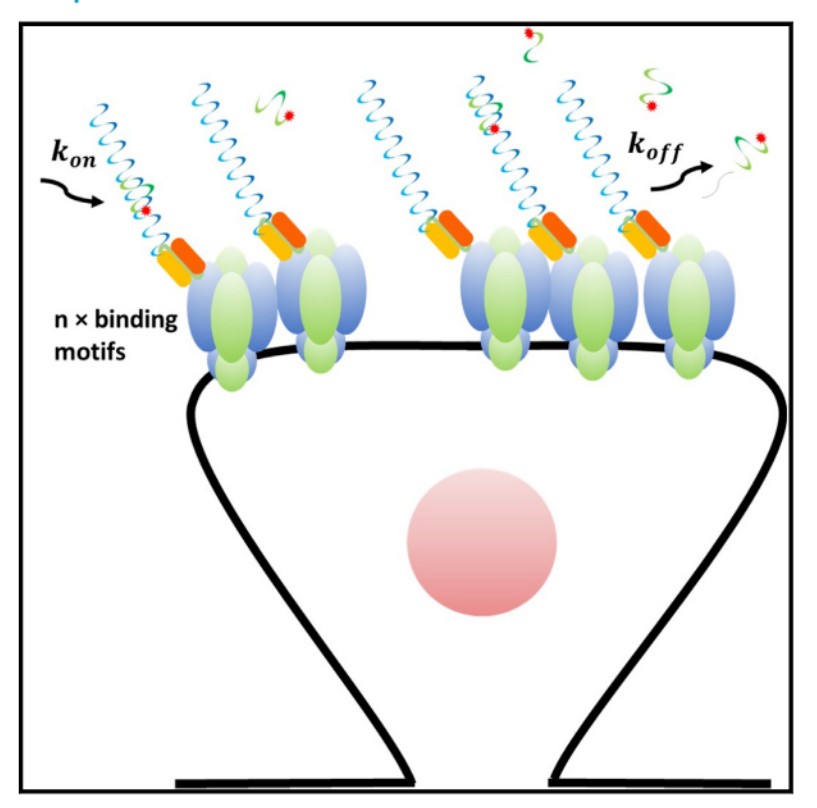


# Quantitative DNA-PAINT imaging of AMPA receptors in live neurons

### Graphical abstract



### **Authors**

Yeoan Youn, Gloria W. Lau, Yongjae Lee, Barun Kumar Maity, Eric Gouaux, Hee Jung Chung, Paul R. Selvin

### Correspondence

selvin@illinois.edu

### In brief

Youn et al. develop a super-resolution imaging technique that can be used for imaging live cells. They apply this technique to observe nanometric spatial distribution and diffusion of neuronal receptors in live neurons under physiological conditions.

### **Highlights**

- A super-resolution imaging technique that can be used for live cells
- Multiple binding motifs (MBMs) in the docker increase speed and stability
- MBMs enable DNA-PAINT imaging in live cultured neurons
- Our results reveal distribution and diffusion of AMPA receptors in live neurons







### **Article**

# Quantitative DNA-PAINT imaging of AMPA receptors in live neurons

Yeoan Youn,<sup>1</sup> Gloria W. Lau,<sup>1</sup> Yongjae Lee,<sup>1</sup> Barun Kumar Maity,<sup>2</sup> Eric Gouaux,<sup>3,4</sup> Hee Jung Chung,<sup>5,6,7</sup> and Paul R. Selvin<sup>1,2,8,\*</sup>

<sup>1</sup>Center for Biophysics and Quantitative Biology, University of Illinois at Urbana-Champaign, Urbana, IL, USA

https://doi.org/10.1016/j.crmeth.2023.100408

**MOTIVATION** Single-molecule localization microscopy can provide nanoscale resolution of molecular structure of biological samples, yet the application of the technique in live samples is limited. Here, we developed a live-cell DNA-PAINT technique to image and quantify neuronal receptor molecules in live hippocampal neurons.

### SUMMARY

DNA-point accumulation for imaging at nanoscale topography (DNA-PAINT) can image fixed biological specimens with nanometer resolution and absolute stoichiometry. In living systems, however, the usage of DNA-PAINT has been limited due to high salt concentration in the buffer required for specific binding of the imager to the docker attached to the target. Here, we used multiple binding motifs of the docker, from 2 to 16, to accelerate the binding speed of the imager under physiological buffer conditions without compromising spatial resolution and maintaining the basal level homeostasis during the measurement. We imaged endogenous  $\alpha$ -amino-3-hydroxy-5-methyl-4-isoxazolepropionic acid receptor (AMPAR) in cultured neurons—critical proteins involved in nerve communication—by DNA-PAINT in 3-dimensions using a monovalent single-chain variable fragment (scFv) to the GluA1 subunit of AMPAR. We found a heterogeneous distribution of synaptic AMPARs:  $\approx$  60% are immobile, primarily in nanodomains, defined as AMPARs that are within 0.3  $\mu$ m of the Homer1 protein in the postsynaptic density; the other  $\sim$ 40% of AMPARs have restricted mobility and trajectory.

### INTRODUCTION

Single-molecule localization microscopy (SMLM) can visualize nanometric structure and dynamics of biological specimen beyond the diffraction limit of light (~250 nm) by localizing the position of individual single molecules. <sup>1–5</sup> Point accumulation for imaging at nanoscale topography (PAINT) is a particular SMLM which generally relies on the transient hybridization of an external fluorescent imager probe with a docker probe that is bound to the protein or object of interest. The (single-molecule) image can then be localized to within a few nanometers when bound and therefore stationary. Repeated hybridizations allow the entire image to be acquired. Most commonly, the donor and imaging probes are made of short single-stranded DNA (ssDNA) that hybridize transiently—hence the name DNA-PAINT (Figure 1A). In PAINT, the fluorophore itself

is made to not blink, and hence imaging does not depend on the photophysics of the dye but rather on the donor and acceptor hybridization rate.6 Hence, DNA-PAINT does not rely on chemical reductants (e.g., MEA or βME) or high-power lasers (~kW/cm²), a common requirement in (d)STORM imaging.7 Also, imager molecules can be replaced from the pool of imagers diffusing in the buffer solution, and therefore the measurement can be sustained over long period of time under oxygenated condition without suffering from photobleaching.8 Using DNA-PAINT, one can quantify the number of molecules by looking at the blinking frequency of the event in a region of interest, even if individual molecules are located closer than the nanometric spatial resolution of the DNA-PAINT image.9 Quantitative PAINT (qPAINT) is then able to count the absolute number of molecules by comparing the frequency rate found with that of a single-molecule frequency.



<sup>&</sup>lt;sup>2</sup>Department of Physics, University of Illinois at Urbana-Champaign, Urbana, IL, USA

<sup>&</sup>lt;sup>3</sup>Vollum Institute, Oregon Health & Science University, Portland, OR, USA

<sup>&</sup>lt;sup>4</sup>Howard Hughes Medical Institute, Portland, OR, USA

<sup>&</sup>lt;sup>5</sup>Department of Molecular and Integrative Physiology, University of Illinois at Urbana-Champaign, Urbana, IL, USA

<sup>&</sup>lt;sup>6</sup>Beckman Institute for Advanced Science and Technology, University of Illinois at Urbana-Champaign, Urbana, IL, USA

<sup>&</sup>lt;sup>7</sup>Neuroscience Program, University of Illinois at Urbana-Champaign, Urbana, IL, USA

<sup>&</sup>lt;sup>8</sup>Lead contact

<sup>\*</sup>Correspondence: selvin@illinois.edu



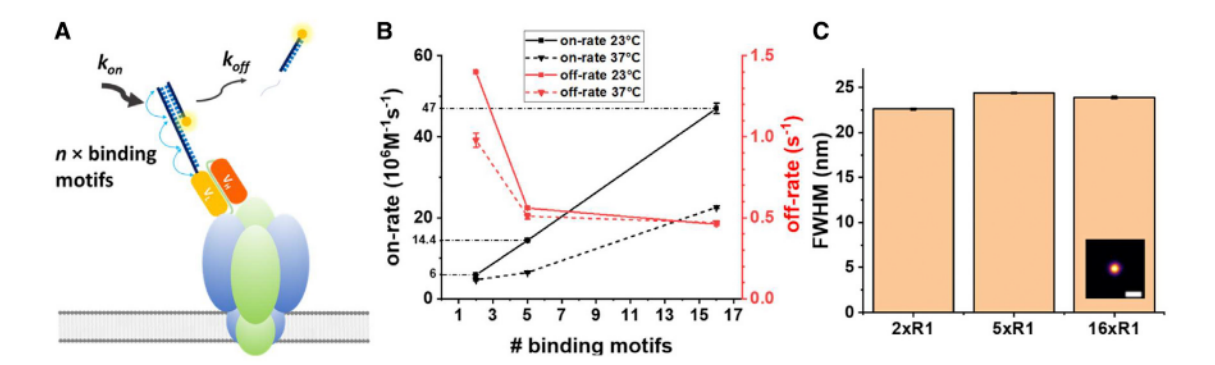


Figure 1. How live-cell DNA-PAINT works

(A) Schematic showing the idea of live-cell DNA-PAINT by using MBMs in docking strand DNA. Multiple binding motifs on a single docker strand increase the binding rate (kon) of the imager and stabilize the binding.

(B) On and off rate of imager (R1\_8nt, 0.64 nM) to the dockers with 2 (2xR1), 5 (5xR1), and 16 (16xR1) binding motifs in physiological buffer ASCF at room temperature (solid lines, n = 15,183, 1,240, and 2,459 immobilized dockers for 2xR1, 5xR, and 16xR1, respectively) and those of R1\_9nt to the dockers at 37°C (dotted lines, n = 1,259, 598, and 516 immobilized dockers for 2xR1, 5xR1, and 16xR1, respectively). Error bars represent SEM. Some error bars are smaller than the symbols. (C) FWHM of single-molecule localization of a surface-immobilized docker molecules over 2,000 s. Inset: representative reconstructed image of single-molecule localizations of one surface immobilized docker. n = 5,856, 5,557, and 1,418 immobilized dockers for 2xR1, 5xR1, and 16xR1, respectively. Scale bar: 100 nm. Error bars represent SEM. Some error bars are smaller than the symbols. See also Videos S1 and S2.

Despite the advantages described above, DNA-PAINT in live cells has been limited to non-physiological conditions. 10,11 The major drawback of DNA-PAINT is its slow image acquisition rate, which is dependent on the binding rate of imager and docker  $(k_{on})$  and the concentration of the imager. To achieve high  $k_{on}$ , the addition of a high concentration of salt (e.g. PBS supplemented with 500 mM NaCl or Tris buffer supplemented with 25-75 mM MaCl<sub>2</sub>) is required to overcome electrical repulsion between the negatively charged imager and docker DNA.8,12 This can lead to deviations from the physiology status, especially for cells that are sensitive to ionic environments, such as neurons. An exception is universal PAINT (uPAINT), which can be done in physiological conditions, uPAINT uses direct binding of fluorescently labeled probe molecules (e.g., immunoglobulin G [lgG], nanobodies) specific to the molecules of interest. However, this variation on the technique is limited by the slow association rate of the probe molecules (e.g., 103-104 M<sup>-1</sup>s<sup>-1</sup> of IgG) and photobleaching of bound probe due to non-exchangeable (~permanent) binding.

Recent advances in the DNA-PAINT technique have improved  $k_{on}$  of the imager-docker strands. Strauss et al. reported that multiple binding motifs (MBMs) on the docker linearly increased the speed of DNA-PAINT imaging.14 It has also been shown that MBMs on DNA origami improve the specificity of binding and reduce photoinduced damage in DNA origami samples, 15 showing the potential of DNA-PAINT for live-cell imaging conditions. 16

α-amino-3-hydroxy-5-methyl-4-isoxazolepropionic acid receptor (AMPAR) is an important neurotransmitter receptor molecule in synaptic plasticity of excitatory synapses of neurons. The efforts to understand the precise location, spatial organization, and diffusion of the receptor have shown heterogeneous distribution of AMPARs not only in spatial localization with respect to the synapse but also in the diffusion of the receptor on the membrane surface. 17-19 Although previous studies have visualized the spatial distribution and the diffusion of single AMPARs, there have been concerns regarding the artifacts

that could be caused by the procedures involved in imaging techniques, such as overexpression<sup>20</sup> of proteins to fuse photoactivatable fluorescence proteins for photoactivation localization microscopy (PALM) imaging, or cross-linking caused by labeling molecules with multivalent tagging molecules (e.g., IgG, streptavidin).<sup>21,22</sup> Therefore, it is important to develop imaging methods that can acquire the spatial organization and can track the movement of AMPARs without causing issues.

Here, we performed live-cell DNA-PAINT imaging of glutamatergic AMPARs on the plasma membrane of live hippocampal neurons under physiological conditions, namely artificial cerebrospinal fluid (ACSF). We measured the binding kinetics of imager to the dockers and have shown that the MBM accelerates the binding rate of the imager to the docker linearly proportional to the number of binding motifs, up to 16 in the overlapping scheme. In addition, the probes consisted of a single-chain variable fragment (scFv) and an MBM docker; importantly, the scFv is a monovalent recombinant small antibody (27 kDa) specific to GluA1, a subunit of AMPARs.<sup>23</sup> Hence, cross-linking, which is potentially a problem with (divalent) antibodies, is avoided. We observed mobile and immobile fraction of AMPARs in synaptic and extrasynaptic regions (less than 2 µm from postsynaptic density [PSD]) of hippocampal neurons. Also, using the quantitative nature of the DNA binding rate,9 we estimated the relative quantity of AMPARs as a function of their spatial distribution and diffusion. It is also possible to use DNA-PAINT over a range of temperatures by varying the length of the imager DNA and hence its unbinding rate.

### **RESULTS**

### MBM improves binding rate and stability of dockerimager in physiological buffer

First, we measured the binding kinetics of docker-imager hybridization in ACSF, a live-cell buffer (see STAR Methods for



chemical composition). Previous studies reported that the binding rate of short DNA oligos is dependent on the salt concentration of the buffer solution. 12 As shown in Figure 1A (also see Videos S1 and S2), the MBM on the docking strand increases the binding rate  $(k_{on})$  so that DNA-PAINT can be performed on a living cell. In the case of the neuron, we used an 8-nt imager, which is long enough when binding the MBM (5xR1 and 16xR1) to track the receptor under physiological conditions (the 2xR1 off rate is  $\sim$ 2x faster than that of 5xR1 and 16xR1; therefore, the trajectory length will be shorter). To show this, we imaged transient binding of an 8-nt imager to a surface-immobilized docker in vitro. This measured the hybridization kinetics of the MBM docker and imager in ACSF. Figure 1B shows  $k_{on}$  of imager R1 increases linearly from 6–47 × 10<sup>6</sup> M<sup>-1</sup>s<sup>-1</sup> from 2-16 binding motifs on the docking strand (2xR1-16xR1). This proves that MBM effectively increases the rate of imager-docker binding at physiological salt concentrations. As the concentration of NaCl in ACSF is about 4x lower than that in the usual buffer used in DNA-PAINT (called Buffer C<sup>6</sup>), the on rate of the imager in ACSF is 3x lower than that in buffer C. However, this rate is still ≈20× faster than traditional DNA-PAINT.8 We also found that the increased number of binding motifs stabilizes the binding of the imager ( $k_{off}$  in Figure 1B). As previously observed, 14 this indicates a potential stabilization of DNA hybridization due to adjacent binding motifs that apparently tends to increase the effective concentration of docking sites. As a result of the stabilization, the binding of the 8-nt imager to the 16x docker has  $\sim$ 2 s long duration compared with  $\sim$ 0.9 s for the 2x docker. 2 s is long enough to visualize trajectories of molecules (see later sections). We also used 9-nt imager lengths (Figure 1B, dotted lines: Table S2), which are necessary for 37°C.

A potential concern due to the elongated length of docker is whether the extra length of the docking strand lowers the resolution of the reconstructed image due to its fluctuations or deviation of the binding sites from its origin. To address this issue, we measured the full-width-half-maximum (FWHM) of the DNA-PAINT image of the surface immobilized docking strand (Figures 1C and S1). The FWHM (corrected for drift) includes the potential effect of an elongated docking strand and thus represents the resolution of the image. We find that the FWHM showed constant value within the range between 2 and 16 binding motifs, implying that the resolution is not compromised due to the long docking strands (Figure 1C). Rather, we observed a slight improvement in resolution with the longer docker, possibly due to the more frequent binding of imager, which results in a reduced SE of localization. Therefore, DNA-PAINT imaging with MBM improves imaging speed without compromising spatial resolution.

### **Imaging AMPARs in live hippocampal neurons**

We next imaged endogenous AMPARs on the plasma membrane surface of live hippocampal neurons. To label endogenous GluA1 containing AMPARs (GluA1-AMPARs), we conjugated scFv and the DNA docker (16xR1) using Sortase-mediated reaction and copper-free click chemistry24,25 (see STAR Methods). The scFv, made specific to GluA1-AMPAR, was developed in the literature,<sup>26</sup> and this method provided a monovalent probe with 1-to-1 labeling stoichiometry, enabling us to label endogenous GluA1-AMPARs. This circumvented overexpression and crosslinking, two common problems in immunostaining and fluorescence imaging. 21,22 Specificity of scFv-16xR1 conjugates was confirmed by co-staining with antibody that stains GluA1 (Abcam, cat #ab174785) and calculating Pearson's correlation coefficient between the antibody and scFv conjugates (Pearson's correlation coefficient [PCC] = 0.31 for entire image and 0.48 for spines only; see STAR Methods and Figure S2).27 GluA1-AMPARs tagged by scFv-16xR1 were visualized by transient binding of fluorescent imager (R1\_8nt-LD655). Collection of imager binding displays the image of surface GluA1-AMPARs in live hippocampal neurons (Figures 2A, 2B, and Video S3). For 3D localization, a cylindrical lens was used to generate astigmatism for axial localization (Figure 2B).<sup>28</sup> The binding of the imager is specific to the docker, as, on average, less than 1 binding was observed in the same region of interest (ROI) per frame without a docker strand (Figure S2D). The frequency of imager binding is constant over the measurement time (200 s imaging; Figure S3A), suggesting that DNA-PAINT is resistant to photobleaching, which may result in loss of information, and that the imaged cells remain homeostatic in terms of the number of GluA1-AMPARs on the membrane surface under imaging condition. Also, the spatial distribution and the diffusion of AMPARs remained constant (Figures S3B-S3D and see later discussion). These results suggest that we can image the receptors on the plasma membrane of live neurons without adversely affecting them.

### GluA1-AMPAR distribution is spatially heterogeneous

We measured the spatial distribution of GluA1-AMPARs in 3-dimensions. As a reference point, we imaged Homer1, which is a protein in the PSD at active excitatory synapses.<sup>29</sup> Endogenous Homer1 was labeled by expressing an intrabody specific to Homer130 fused to a photoactivatable fluorescent protein (mGeos<sup>31</sup>). Super-resolution can therefore be achieved by taking a PALM2 image of mGeos.18 We measured the distance between GluA1-AMPARs and the clusters of the nearest Homer1 neighbor, showing the distribution of GluA1-AMPARs with respect to the location of synapses (Figure 2C). In Figure 2C, the cumulative distribution of GluA1-AMPARs shows that the slope from the 0-0.3  $\mu$ m region is  $\sim$ 4× steeper than in the 0.3-2  $\mu m$  range. Hence, the density of GluA1-AMPAR in this region is higher than the later range. We defined this 0-0.3 μm region as "synaptic" and the 0.3-2 µm region as "extrasynaptic." This heterogeneous distribution indicates that (1) GluA1-AMPARs are enriched in the area of the synaptic region and (2) there are a number of extra-synaptic AMPARs as reported previously. 18,19,32,33

### Different diffusion behavior between GluA1-AMPARs in synaptic and extra-synaptic regions

Then, we looked at how the diffusion of GluA1-AMPARs depends on the location of the receptors—in the synaptic region (0-0.3 μm from Homer1), where the density of GluA1-AMPAR is  $\sim$ 4× higher, versus that of extra-synaptic region (0.3–2  $\mu$ m) from Homer1). We calculated and plotted the diffusion coefficient versus the range of trajectories of single GluA1-AMPAR molecules by obtaining the mean-squared displacement (Figures 2D-2F; Table 1). We found that there are two distinct



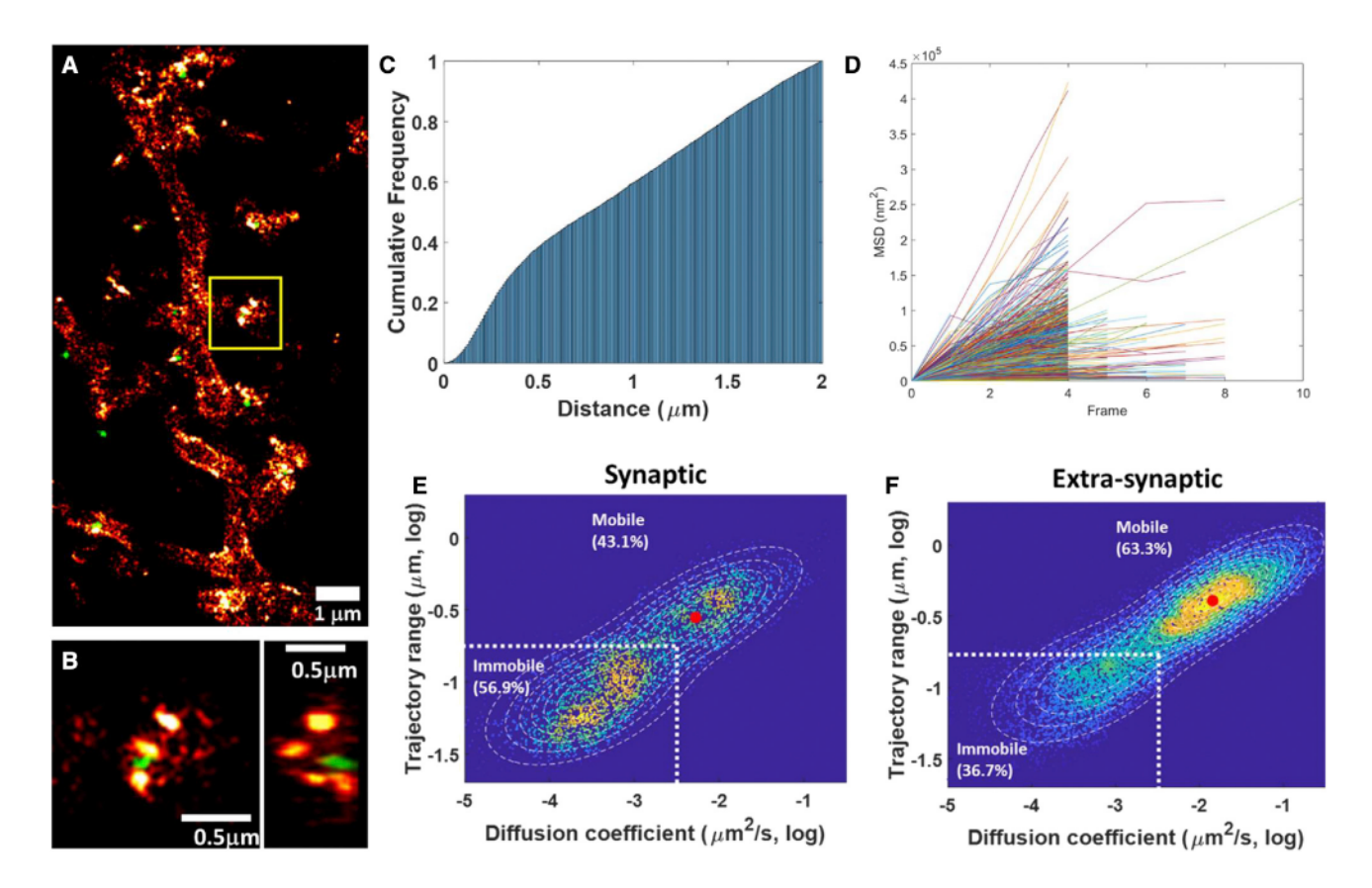


Figure 2. Live-cell 3D-DNA-PAINT image of endogenous GluA1-AMPAR in live hippocampal neurons

Images were taken with 1 nM R1\_8nt-LD655 imager.

- (A) Reconstructed DNA-PAINT image of GluA1-AMPARs (red hot) and Homer1 (green).
- (B) Magnified view of highlighted spine of the neuron in the yellow square in the lateral (x-y, left) and vertical projection (y-z, right).
- (C) Cumulative frequency of the radial distribution of GluA1-AMPAR molecules with respect to nearest postsynaptic marker, Homer1.
- (D) Example of mean-squared displacement (MSD) curve of GluA1-AMPARs (n = 4,102 trajectories).

(E and F) Density scatterplot and histogram showing the diffusion coefficient and trajectory range of 3D trajectories of GluA1-AMPARs in synaptic region (E) and juxta-synaptic region (F). The percentage is estimated by using a Gaussian mixture model with 2 components. Red dots indicate the center of mobile population (n = 9 cells from 4 independent batches of cell cultures, 9,780 trajectories). See also Video S3.

population of GluA1-AMPARs in both the synaptic and extrasynaptic regions. By fitting the diffusion coefficient and the trajectory range with two 2-dimensional Gaussian functions, we distinguish them into two groups, a mobile and an immobile group of receptors, for both the synaptic and extra-synaptic populations. To define "mobile" and "immobile" groups, we must first calculate the lowest diffusion coefficient and the shortest trajectory range we could detect. The limits of detection (LODs) are based on the localization accuracy—anything below these values for a given diffusion constant or trajectory range will be defined as immobile. The LOD was calculated based on the dimension that has the poorest localization accuracy-in this case, the axial dimension ( $\sim$ 75 nm), which was  $\sim$ 3× poorer than the lateral accuracy. The lowest detectable diffusion coefficient was  $0.003 (=10^{-2.5}) \mu m^2/s$ , and the shortest trajectory range was 0.18 (= $10^{-0.75}$ )  $\mu m$ . Therefore, the Gaussian distributions whose mean values were below the values were defined as immobile and above these values were defined as mobile (see

STAR Methods for details). Figure 2E shows the characteristics of the diffusion of GluA1-AMPARs in the synaptic region and Figure 2F in the extra-synaptic region (values can be found in Table 1).

Given that we defined these two groups, we find that both mobile and immobile receptors in the synaptic region diffuse more slowly and over a shorter range than those of the extra-synaptic receptors. We estimated the relative amount of each group, based on the principle of qPAINT,9 by looking at the detection frequency. The result showed that there is a greater fraction of immobile GluA1-AMPARs in the synaptic region (Figure 2E; 56.9%) than that in extra-synaptic region (Figure 2F; 36.7%). Also, the diffusion of mobile receptors is  $\sim 2.5 \times$  slower in the synaptic region than in the extra-synaptic region (average  $D_{\text{mobile-syn}} = 0.006 (10^{-2.21}) \, \mu\text{m}^2\text{/s compared with } D_{\text{mobile-extra}} =$  $0.015 (10^{-1.82}) \mu m^2/s$ ). This observation suggests that in synapses, GluA1-AMPARs are largely immobile, and even for mobile receptors, the diffusion is hindered. Previous studies have

### Article



Table 1. Diffusion coefficient and trajectory range of GluA1-AMPARs

Region	Mobile		Immobile	
	Diff. coeff. (μm²/s)	Traj. range (μm)	Diff. coeff. (μm²/s)	Traj. range (μm)
Synaptic	10 <sup>-2.21 ± 0.37</sup>	10 <sup>-0.53 ± 0.06</sup>	10 <sup>-3.56 ± 0.37</sup>	10 <sup>-1.12 ± 0.05</sup>
Juxta-synaptic	$10^{-1.82 \pm 0.36}$	$10^{-0.38 \pm 0.06}$	$10^{-3.37 \pm 0.40}$	$10^{-0.96 \pm 0.06}$

shown that AMPARs are immobilized in the "slots" inside of synapses by the molecular interaction with scaffolding proteins (e.g., PSD-95) and transmembrane AMPAR regulatory proteins (e.g., stargazin), resulting in half of GluA2-AMPARs being immobile in synapses as measured by uPAINT. (We found 57% of GluA1-AMPARs.) The crowded environment in PSD 35,36 and the recent finding of density-dependent multimerization of AMPARs may explain our observation of restricted mobility of diffusive GluA1-AMPARs in the synaptic region.

### **GluA1-AMPARs form synaptic nanodomains**

Finally, we investigated subsynaptic localization and diffusion of GluA1-AMPARs. In the representative image of a spine (Figure 3A) with Homer1 (green) and GluA1-AMPARs (red hot), the distribution of GluA1-AMPAR is heterogeneous. In Figure 3A1, three small domains (highlighted with dashed ellipses) are enriched in GluA1-AMPARs-these area are called synaptic nanodomains. 17 The trajectories of the GluA1-AMPARs located in the nanodomains are greatly restricted: Figure 3A2 shows trajectories of synaptic GluA1-AMPARs, and Figure 3A3 highlights that subset of trajectories of GluA1-AMPARs that are immobile, i.e., those that have D <  $10^{-2.5}$   $\mu m^2/s$ . We found that the immobile receptors are confined the synaptic nanodomains ≈ 1203 nm3 (Figure 3D), consistent with a previous report. 17 To see the distribution of the immobile receptors with respect to the synapse, we plotted the diffusion constant versus distance from Homer1 (Figure 3B). We found that the nanodomains are greatly confined to the synaptic region, which we defined as 0-0.3 μm from Homer1. Measuring the fraction of GluA1-AMPARs in nanodomains as a function of distance from the nearest Homer1, we found that ~60% of GluA1-AMPARs are in nanodomains in the synaptic region (Figure 3C). The fraction in nanodomains rapidly decreases and goes down to  $\sim$ 30% after 1  $\mu$ m distance (in 3D) from the Homer1. The fraction of GluA1-AMPARs found in the extra-synaptic region could be due to immobilization in endocytic zones existing in close proximity of Homer1.38

### DISCUSSION

In summary, we developed live-cell super-resolution imaging technique via DNA-PAINT: it shows the position, movement, and quantity of surface receptors in live neurons. To our knowledge, this is the first demonstration of DNA-PAINT imaging of living cells under physiological condition. Overlapping MBMs improves the speed of imaging without sacrificing resolution or signal-to-background ratio. We were able to reconstruct the image of AMPARs in live neurons with ~30 nm lateral and ~75 nm axial resolution (Figures S1E and S1F). Repetition of binding

sequence (e.g., ...TCCTCC ...; Table S1) provides additional benefit for tuning the binding of imager-docker due to different experimental conditions or requirements (e.g., temperature, length of trajectory). We chose an 8-nt imager, which binds for about 2 s, to image trajectories of GluA1-AMPARs at room temperature with minimal photobleaching of the bound imager. However, it is possible to choose a longer imager (simply by adding one nucleotide) to observe as long trajectories as the photostability of the dye allows or, alternatively, to perform the experiment at 37°C, which is known to be more physiological. We have shown that the binding and exchange of imagers can be obtained at 37°C using a 9-nt imager (Figure 1B, dotted lines), and imaging and tracking of GluA1-AMPARs at 37°C using a 9-nt imager was done (Figure S4).

By using monovalent small antibody scFv-docker conjugates, we labeled and imaged endogenous GluA1-AMPARs without overexpression and cross-linking of the molecules. We found that GluA1-AMPARs are enriched near the synapse showing higher distribution within 0.3 µm (in 3-dimensions) from Homer1, a protein of the PSD. qPAINT also enabled accurate counting of molecules. For the images acquired for live neurons, the coefficient of variation ( $C_V = \sigma/\mu$ , SD/mean) of the number of detected events is calculated to estimate the counting error of qPAINT approach (Figure S3E). Consistent with a previous report,9 the coefficient of accuracy decreases as more frames are collected. By fitting with equation ( $C_v = A(1/[x + B])$ ), where x is number of frames and A and B are fitting constants) and extrapolating, we found that the counting error of our images is ~1.7% with 2,000 frames of measurement. By tracking single receptors, we found that half of GluA1-AMPARs in synapse are immobile under basal condition. This immobile fraction of GluA1-AMPARs exists in synaptic nanodomains where the receptors enrich and are potentially aligned to the presynaptic glutamate release site as reported. 17,39 The observations are consistent with previous reports, proving that AMPARs form nanometric organization without causing overexpression or hindering molecular diffusion by cross-linking. The results show that endogenous GluA1-containing receptors are also involved in the formation of the nanodomains. These findings support that live-cell DNA-PAINT is suitable technique for studying subdiffraction-limited localization and diffusion of receptor molecules on the membrane of live neurons with minimal perturbation.

### Limitations of the study

At present, the technique is currently limited to image target molecules on the membrane surface. <sup>10,11,13</sup> To extend the technique to cytosolic targets, (1) methods for internalization of probes must be developed, and (2) non-specific binding of the probe inside the cells, especially to the nucleus of the cell, needs to be



### **Cell Reports Methods** Article

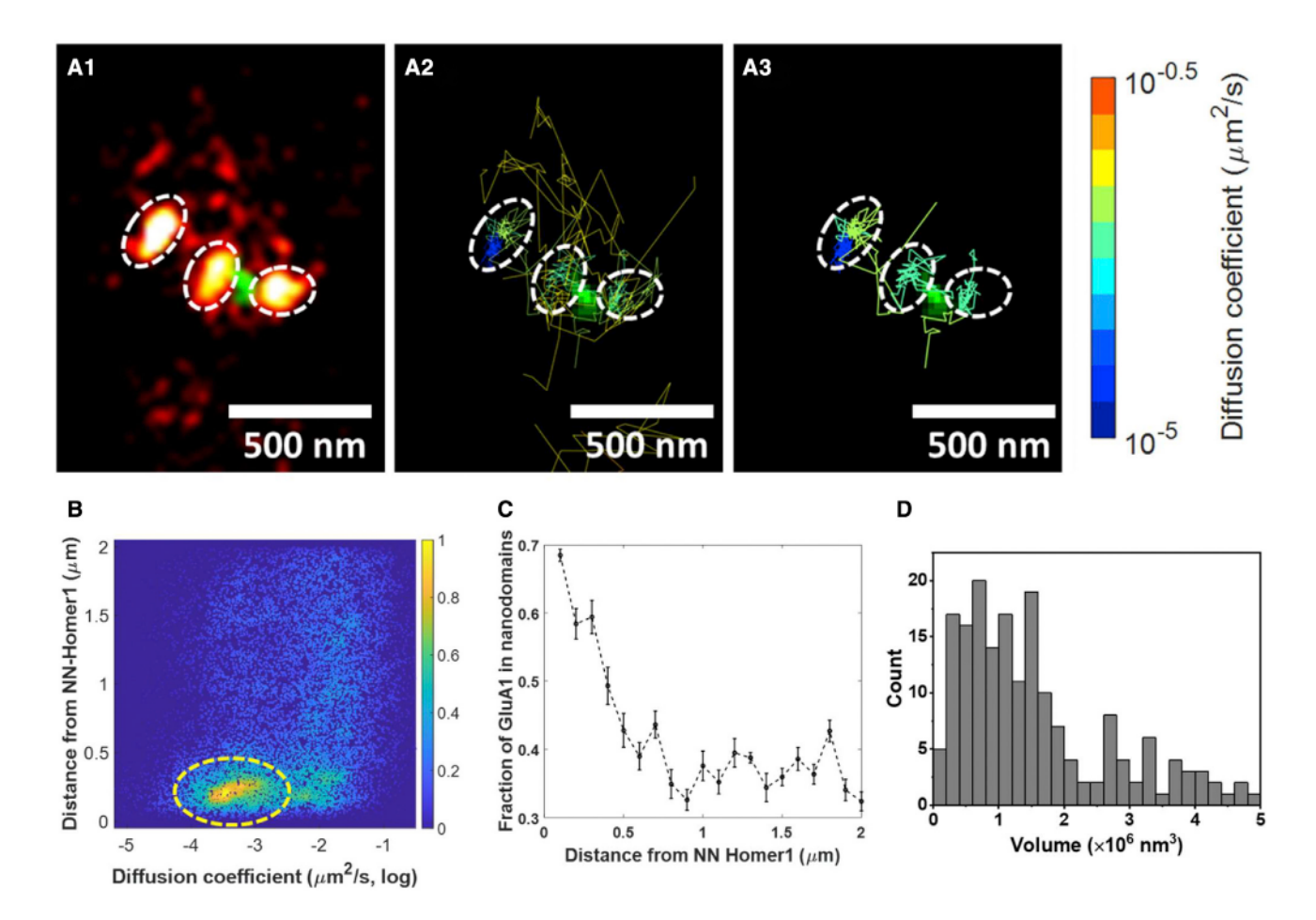


Figure 3. Synaptic nanodomains of GluA1-AMPARs

(A1-A3) (A1) Representative image of synaptic GluA1-AMPARs (red hot) with respect to Homer1 (green). Nanodomains that correspond to the high-density region of GluA1-AMPARs are highlighted with dashed ellipses. (A2) Trajectories of GluA1-AMPARs in the image. (A3) The trajectories of GluA1-AMPARs with restricted  $mobility (D < 10^{-2.5} \, \mu m^2/s) \, were \, plotted. \, Trajectories \, are shown \, as \, solid \, lines \, with \, the \, color \, that \, indicates \, the \, diffusion \, coefficient \, of \, the \, trajectory \, according \, to \, the \, trajectory \, according to \, the \, trajectory \,$ color bar. Scale bar: 500 nm for (A1)-(A3).

- (B) Density scatterplot showing diffusion coefficient of GluA1-AMPAR as a function of distance from nearest-neighbor Homer1 (NN-Homer1). Color bar represents the density of data points.
- (C) Fraction of GluA1-AMPARs in nanodomains is plotted as a function of distance from NN-Homer1. Error bars represent SEM (n = 9 cells from 4 independent batches of cell cultures).
- (D) Size distribution of synaptic nanodomains.

blocked or replaced with alternative probes such as peptide<sup>40,41</sup> or artificial nucleic acid probes such as peptide nucleic acid (PNA)<sup>42</sup> or left-handed DNA.<sup>43</sup>

### **STAR**\*METHODS

Detailed methods are provided in the online version of this paper and include the following:

- KEY RESOURCES TABLE
- RESOURCE AVAILABILITY
  - Lead contact
  - Materials availability
  - Data and code availability
- EXPERIMENTAL MODEL AND SUBJECT DETAILS
- METHOD DETAILS

- Hippocampal neuron culture and transfection
- O Mutagenesis, expression, and purification of anti-GluA1 scFv (LPETGG-6xHis)
- Sortase A mediated conjugation and copper-free click chemistry of scFv-docker
- Labeling DNA oligo with fluorophores
- Microscope setup
- Buffers
- DNA-PAINT image acquisition
- scFv specificity experiments
- QUANTIFICATION AND STATISTICAL ANALYSIS
  - Single molecule localization
  - O Calculation of kon and koff of imager to the surface immobilized docker in vitro
  - Diffusion coefficient and trajectory range
  - Nanodomains



### SUPPLEMENTAL INFORMATION

Supplemental information can be found online at https://doi.org/10.1016/i. crmeth.2023.100408.

#### **ACKNOWLEDGMENTS**

This work was supported by NIH/NINDS grants R01NS038631 to E.G. and R01 NS100019 to P.R.S. and H.J.C. and NSF Physics Frontier Center grant PHY-143012 to P.R.S. E.G. is an investigator of the Howard Hughes Medical Institute.

#### **AUTHOR CONTRIBUTIONS**

Y.Y., with assistance from G.W.L., Y.L., and B.K.M., performed experiments, analyzed the data, and, along with H.J.C., E.G., and P.R.S., participated in writing the manuscript. E.G. also provided necessary reagents. H.J.C. and P.R.S also designed the experiments and analyzed data.

### **DECLARATION OF INTERESTS**

The authors declare no competing interests.

Received: May 9, 2022 Revised: September 25, 2022 Accepted: January 25, 2023 Published: February 16, 2023

#### REFERENCES

- 1. Yildiz, A., Forkey, J.N., McKinney, S.A., Ha, T., Goldman, Y.E., and Selvin, P.R. (2003). Myosin V walks hand-over-hand: single fluorophore imaging with 1.5-nm localization. Science 300, 2061-2065. https://doi.org/10. 1126/science.1084398.
- 2. Betzig, E., Patterson, G.H., Sougrat, R., Lindwasser, O.W., Olenych, S., Bonifacino, J.S., Davidson, M.W., Lippincott-Schwartz, J., and Hess, H.F. (2006). Imaging intracellular fluorescent proteins at nanometer resolution. Science 313, 1642-1645. https://doi.org/10.1126/science. 1127344.
- 3. Rust, M.J., Bates, M., and Zhuang, X. (2006). Sub-diffraction-limit imaging by stochastic optical reconstruction microscopy (STORM). Nat. Methods 3, 793-795. https://doi.org/10.1038/nmeth929.
- 4. Hess, S.T., Girirajan, T.P.K., and Mason, M.D. (2006). Ultra-high resolution imaging by fluorescence photoactivation localization microscopy. Biophys. J. 91, 4258-4272. https://doi.org/10.1529/biophysj.106.091116.
- 5. Heilemann, M., van de Linde, S., Schüttpelz, M., Kasper, R., Seefeldt, B., Mukherjee, A., Tinnefeld, P., and Sauer, M. (2008). Subdiffraction-resolution fluorescence imaging with conventional fluorescent probes. Angew. Chem. Int. Ed. Engl. 47, 6172-6176. https://doi.org/10.1002/anie.
- 6. Schnitzbauer, J., Strauss, M.T., Schlichthaerle, T., Schueder, F., and Jungmann, R. (2017). Super-resolution microscopy with DNA-PAINT. Nat. Protoc. 12, 1198-1228. https://doi.org/10.1038/nprot.2017.024.
- 7. Diekmann, R., Kahnwald, M., Schoenit, A., Deschamps, J., Matti, U., and Ries, J. (2020). Optimizing imaging speed and excitation intensity for single-molecule localization microscopy. Nat. Methods 179, 909-912. https://doi.org/10.1038/s41592-020-0918-5.
- 8. Jungmann, R., Steinhauer, C., Scheible, M., Kuzyk, A., Tinnefeld, P., and Simmel, F.C. (2010). Single-molecule kinetics and super-resolution microscopy by fluorescence imaging of transient binding on DNA origami. Nano Lett. 10, 4756-4761. https://doi.org/10.1021/nl103427w.
- 9. Jungmann, R., Avendaño, M.S., Dai, M., Woehrstein, J.B., Agasti, S.S., Feiger, Z., Rodal, A., and Yin, P. (2016). Quantitative super-resolution imaging with qPAINT. Nat. Methods 13, 439-442. https://doi.org/10.1038/ nmeth.3804.

- 10. Strauss, S., Nickels, P.C., Strauss, M.T., Jimenez Sabinina, V., Ellenberg, J., Carter, J.D., Gupta, S., Janjic, N., Jungmann, R., Sabinina, V.J., et al. (2018). Modified aptamers enable quantitative sub-10-nm cellular DNA-PAINT imaging. Nat. Methods 15, 685-688. https://doi.org/10.1038/ s41592-018-0105-0.
- 11. Brockman, J.M., Su, H., Blanchard, A.T., Duan, Y., Meyer, T., Quach, M.E., Glazier, R., Bazrafshan, A., Bender, R.L., Kellner, A.V., et al. (2020). Live-cell super-resolved PAINT imaging of piconewton cellular traction forces. Nat. Methods 17, 1018-1024. https://doi.org/10.1038/s41592-020-0929-2.
- 12. Cisse, I.I., Kim, H., and Ha, T. (2012). A rule of seven in Watson-Crick basepairing of mismatched sequences. Nat. Struct. Mol. Biol. 19, 623-627. https://doi.org/10.1038/nsmb.2294.
- 13. Giannone, G., Hosy, E., Levet, F., Constals, A., Schulze, K., Sobolevsky, A.I., Rosconi, M.P., Gouaux, E., Tampé, R., Choquet, D., and Cognet, L. (2010). Dynamic superresolution imaging of endogenous proteins on living cells at ultra-high density. Biophys. J. 99, 1303-1310. https://doi.org/10. 1016/j.bpj.2010.06.005.
- 14. Strauss, S., and Jungmann, R. (2020). Up to 100-fold speed-up and multiplexing in optimized DNA-PAINT. Nat. Methods 17, 789-791. https://doi. org/10.1038/s41592-020-0869-x.
- 15. Clowsley, A.H., Kaufhold, W.T., Lutz, T., Meletiou, A., Di Michele, L., and Soeller, C. (2021). Repeat DNA-PAINT suppresses background and nonspecific signals in optical nanoscopy. Nat. Commun. 12, 501-510. https://doi.org/10.1038/s41467-020-20686-z.
- 16. Stehr, F., Stein, J., Bauer, J., Niederauer, C., Jungmann, R., Ganzinger, K., and Schwille, P. (2021). Tracking single particles for hours via continuous DNA-mediated fluorophore exchange. Nat. Commun. 12, 4432-4438. https://doi.org/10.1038/s41467-021-24223-4.
- 17. Nair, D., Hosy, E., Petersen, J.D., Constals, A., Giannone, G., Choquet, D., and Sibarita, J.-B. (2013). Super-resolution imaging reveals that AMPA receptors inside synapses are dynamically organized in nanodomains regulated by PSD95. J. Neurosci. 33, 13204-13224. https://doi.org/10.1523/ JNEUROSCI.2381-12.2013.
- 18. Lee, S.H., Jin, C., Cai, E., Ge, P., Ishitsuka, Y., Teng, K.W., de Thomaz, A.A., Nall, D., Baday, M., Jeyifous, O., et al. (2017). Super-resolution imaging of synaptic and extra-synaptic AMPA receptors with different-sized fluorescent probes. Elife 6, e27744. https://doi.org/10.7554/eLife.27744.
- 19. MacGillavry, H.D., Song, Y., Raghavachari, S., and Blanpied, T.A. (2013). Nanoscale scaffolding domains within the postsynaptic density concentrate synaptic AMPA receptors. Neuron 78, 615-622. https://doi.org/10. 1016/J.NEURON.2013.03.009.
- 20. Hamad, M.I.K., Ma-Högemeier, Z.L., Riedel, C., Conrads, C., Veitinger, T., Habijan, T., Schulz, J.-N., Krause, M., Wirth, M.J., Hollmann, M., and Wahle, P. (2011). Cell class-specific regulation of neocortical dendrite and spine growth by AMPA receptor splice and editing variants. Development 138, 4301-4313. https://doi.org/10.1242/DEV.071076.
- 21. Sograte-Idrissi, S., Schlichthaerle, T., Duque-Afonso, C.J., Alevra, M., Strauss, S., Moser, T., Jungmann, R., Rizzoli, S.O., and Opazo, F. (2020). Circumvention of common labelling artefacts using secondary nanobodies. Nanoscale 12, 10226-10239. https://doi.org/10.1039/
- 22. Penn, A.C., Zhang, C.L., Georges, F., Royer, L., Breillat, C., Hosy, E., Petersen, J.D., Humeau, Y., and Choquet, D. (2017). Hippocampal LTP and contextual learning require surface diffusion of AMPA receptors. Nature 549, 384-388. https://doi.org/10.1038/nature23658.
- 23. Yu, J., Rao, P., Clark, S., Mitra, J., Ha, T., and Gouaux, E. (2021). Hippocampal AMPA receptor assemblies and mechanism of allosteric inhibition. Nature 594, 448-453. https://doi.org/10.1038/s41586-021-03540-0.
- 24. Guimaraes, C.P., Witte, M.D., Theile, C.S., Bozkurt, G., Kundrat, L., Blom, A.E.M., and Ploegh, H.L. (2013). Site-specific C-terminal and internal loop labeling of proteins using sortase-mediated reactions. Nat. Protoc. 8, 1787-1799. https://doi.org/10.1038/nprot.2013.101.



- 25. Fabricius, V., Lefèbre, J., Geertsema, H., Marino, S.F., and Ewers, H. (2018). Rapid and efficient C-terminal labeling of nanobodies for DNA-PAINT. J. Phys. D Appl. Phys. 51, 474005. https://doi.org/10.1088/1361-6463/aae0e2.
- 26. Zhao, Y., Chen, S., Swensen, A.C., Qian, W.J., and Gouaux, E. (2019). Architecture and subunit arrangement of native AMPA receptors elucidated by cryo-EM. Science 364, 355-362. https://doi.org/10.1126/SCIENCE. AAW8250/SUPPL\_FILE/AAW8250\_ZHAO\_SM.PDF.
- 27. Dunn, K.W., Kamocka, M.M., and McDonald, J.H. (2011). A practical guide to evaluating colocalization in biological microscopy. Am. J. Physiol. Cell Physiol. 300, 723-742. https://doi.org/10.1152/AJPCELL.00462.2010/ ASSET/IMAGES/LARGE/ZH00041165590009.JPEG.
- 28. Huang, B., Wang, W., Bates, M., and Zhuang, X. (2008). Three-dimensional super-resolution imaging by stochastic optical reconstruction microscopy. Science 319, 810-813. https://doi.org/10.1126/science. 1153529.
- 29. Clifton, N.E., Trent, S., Thomas, K.L., and Hall, J. (2019). Regulation and function of activity-dependent homer in synaptic plasticity. Mol. Neuropsychiatry 5, 147-161. https://doi.org/10.1159/000500267.
- 30. Dong, J.X., Lee, Y., Kirmiz, M., Palacio, S., Dumitras, C., Moreno, C.M., Sando, R., Santana, L.F., Südhof, T.C., Gong, B., et al. (2019). A toolbox of nanobodies developed and validated for use as intrabodies and nanoscale immunolabels in mammalian brain neurons. Elife 8, e48750. https:// doi.org/10.7554/eLife.48750.
- 31. Chang, H., Zhang, M., Ji, W., Chen, J., Zhang, Y., Liu, B., Lu, J., Zhang, J., Xu, P., and Xu, T. (2012). A unique series of reversibly switchable fluorescent proteins with beneficial properties for various applications. Proc. Natl. Acad. Sci. USA. 109, 4455-4460. https://doi.org/10.1073/PNAS. 1113770109/SUPPL\_FILE/PNAS.1113770109\_SI.PDF.
- 32. Bartol, T.M., Goncalves, J., Camus, C., Levet, F., Menegolla, A.P., Sejnowski, T.J., Sibarita, J.B., Vivaudou, M., Hosy, E., Choquet, D., et al. (2020). Nanoscale co-organization and coactivation of AMPAR, NMDAR, and mGluR at excitatory synapses. Proc. Natl. Acad. Sci. USA. 117, 14503-14511. https://doi.org/10.1073/pnas.1922563117.
- 33. Tardin, C., Cognet, L., Bats, C., Lounis, B., and Choquet, D. (2003). Direct imaging of lateral movements of AMPA receptors inside synapses. EMBO J. 22, 4656-4665. https://doi.org/10.1093/emboj/cdg463.
- 34. Bats, C., Groc, L., and Choquet, D. (2007). The interaction between stargazin and PSD-95 regulates AMPA receptor surface trafficking. Neuron 53, 719-734. https://doi.org/10.1016/J.NEURON.2007.01.030.
- 35. Gupta, R. (2018). Self-crowding of AMPA receptors in the excitatory postsynaptic density can effectuate anomalous receptor sub-diffusion, PLoS Comput. Biol. 14, e1005984. https://doi.org/10.1371/JOURNAL.PCBI. 1005984
- 36. Li, T.P., Song, Y., MacGillavry, H.D., Blanpied, T.A., and Raghavachari, S. (2016). Protein crowding within the postsynaptic density can impede the

- escape of membrane proteins. J. Neurosci. 36, 4276-4295. https://doi. ora/10.1523/JNEUROSCI.3154-15.2016.
- 37. Morise, J., Suzuki, K.G.N., Kitagawa, A., Wakazono, Y., Takamiya, K., Tsunoyama, T.A., Nemoto, Y.L., Takematsu, H., Kusumi, A., and Oka, S. (2019). AMPA receptors in the synapse tumover by monomer diffusion. Nat. Commun. 10, 5245. https://doi.org/10.1038/s41467-019-13229-8.
- 38. Petrini, E.M., Lu, J., Cognet, L., Lounis, B., Ehlers, M.D., and Choquet, D. (2009). Endocytic trafficking and recycling maintain a pool of mobile surface AMPA receptors required for synaptic potentiation. Neuron 63, 92-105. https://doi.org/10.1016/j.neuron.2009.05.025.
- 39. Tang, A.H., Chen, H., Li, T.P., Metzbower, S.R., MacGillavry, H.D., and Blanpied, T.A. (2016). A trans-synaptic nanocolumn aligns neurotransmitter release to receptors. Nature 536, 210-214. https://doi.org/10. 1038/nature19058.
- 40. Eklund, A.S., Ganji, M., Gavins, G., Seitz, O., and Jungmann, R. (2020). Peptide-PAINT super-resolution imaging using transient coiled coil interactions. Nano Lett. 20, 6732-6737. https://doi.org/10.1021/acs.nanolett. 0c02620.
- 41. Oi, C., Gidden, Z., Holyoake, L., Kantelberg, O., Mochrie, S., Horrocks, M.H., and Regan, L. (2020). LIVE-PAINT allows super-resolution microscopy inside living cells using reversible peptide-protein interactions. Commun. Biol. 3, 458. https://doi.org/10.1038/s42003-020-01188-6.
- 42. Guo, S.M., Veneziano, R., Gordonov, S., Li, L., Danielson, E., Perez de Arce, K., Park, D., Kulesa, A.B., Wamhoff, E.C., Blainey, P.C., et al. (2019). Multiplexed and high-throughput neuronal fluorescence imaging with diffusible probes. Nat. Commun. 10, 4377. https://doi.org/10.1038/ s41467-019-12372-6.
- 43. Geertsema, H.J., Aimola, G., Fabricius, V., Fuerste, J.P., Kaufer, B.B., and Ewers, H. (2021). Left-handed DNA-PAINT for improved super-resolution imaging in the nucleus. Nat. Biotechnol. 39, 551-554. https://doi.org/10. 1038/s41587-020-00753-y.
- 44. Ovesný, M., Křížek, P., Borkovec, J., Švindrych, Z., and Hagen, G.M. (2014). ThunderSTORM: a comprehensive ImageJ plug-in for PALM and STORM data analysis and super-resolution imaging. Bioinformatics 30. 2389-2390. https://doi.org/10.1093/BIOINFORMATICS/BTU202.
- 45. Lee, S.H., Baday, M., Tjioe, M., Simonson, P.D., Zhang, R., Cai, E., and Selvin, P.R. (2012). Using fixed fiduciary markers for stage drift correction. Opt Express 20, 12177-12183. https://doi.org/10.1364/OE.20.012177.
- 46. Youn, Y., Ishitsuka, Y., Jin, C., and Selvin, P.R. (2018). Thermal nanoimprint lithography for drift correction in super-resolution fluorescence microscopy. Opt Express 26, 1670-1680. https://doi.org/10.1364/OE.26. 001670.
- 47. Crocker, J.C., and Grier, D.G. (1996). Methods of digital video microscopy for colloidal studies. J. Colloid Interface Sci. 179, 298-310. https:// physics.nyu.edu/grierlab/methods3c/.



### **STAR**\*METHODS

### **KEY RESOURCES TABLE**

REAGENT or RESOURCE	SOURCE	IDENTIFIER
Antibodies		
mouse αGluA1 antibody	Abcam	ab174785; RRID: AB_2920893
Rhodamine (TRITC)-conjugated AffiniPure F(ab')₂ Fragment Goat Anti-Mouse IgG (H + L)	Jackson ImmunoResearch	115-006-062; RRID: AB_2338470
Bacterial and virus strains		
B21(DE3)	NEB	C2527H
Chemicals, peptides, and recombinant proteins		
antiGluA1 scFv	This paper, Yu et al. <sup>23</sup>	N/A
Experimental models: Cell lines		
Primary rat hippocampal neuron culture	Charles River	CD 001
Oligonucleotides		
2xR1	IDT	See Table S1
5xR1	IDT	See Table S1
16xR1	IDT	See Table S1
R1_8nt	IDT	See Table S1
R1_9nt	IDT	See Table S1
Software and algorithms		
MATLAB scripts	Lee et al. 18 and this paper	Mendeley Data: https://doi.org/10.17632/ 6dj3yx6xwg.1

### RESOURCE AVAILABILITY

### Lead contact

Further information and requests for resources and reagents should be directed to and will be fulfilled by the lead contact, Paul R. Selvin (selvin@illinois.edu).

### **Materials availability**

All unique/stable reagents generated in this study are available from the lead contact with a completed materials transfer agreement.

### Data and code availability

- All data reported in this paper will be shared by the lead contact upon request.
- All original code and representative raw images are deposited on Mendeley Data and publicly available as of the date of publication. (Mendeley Data: https://doi.org/10.17632/6dj3yx6xwg.1).
- Any additional information required to reanalyze the data reported in this paper is available from the lead contact upon request.

### **EXPERIMENTAL MODEL AND SUBJECT DETAILS**

Both male and female E19 rat embryo from CD 001 timed pregnant rat was used for primary hippocampal neuron culture. The procedures involving animal care, euthanasia and dissection are performed in accordance with the guidelines and regulations set forth by the Institutional Animal Care and Use Committee at the University of Illinois at Urbana-Champaign.

### **METHOD DETAILS**

### Hippocampal neuron culture and transfection

Primary hippocampal neurons were prepared from E19 rat embryo according to UIUC guidelines. Timed-pregnant rats were euthanized in CO2 gas chamber and decapitated to obtain embryos. The brains were removed from the pups and hippocampi were cut



from the brains after removing meninges. Hippocampal tissues were incubated in 3 mg/mL protease at 37°C for 8 min, then dissociated into single cells via trituration with polished Pasteur pipettes. The number of cells was counted by using hemacytometer and 2×10<sup>5</sup> cells were seeded on a PLL-coated 25 mm coverslip in plating media (MEM supplemented with 10% FBS, 0.45% (w/v) D-glucose, 25 μM L-glutamine, 1 mM sodium pyruvate, and penicillin/streptomycin). In 4 h, after cells attached to the coverslips surface, the culture media was exchanged into maintenance media (neurobasal supplemented with B27, 0.5 mM L-glutamate and penicillin/streptomycin). The cells were keep cultured at 37°C with 5% CO2. On days in vitro (DIV) 12-13, 1 µg of each cDNA was (co-)transfected using Lipofectamine 2000 according to manufacturer's instruction. Prepared cells expressing the proteins were imaged on DIV 15-17.

### Mutagenesis, expression, and purification of anti-GluA1 scFv (LPETGG-6xHis)

The plasmid construct for anti-GluA1 scFv was kindly gifted by Eric Gouaux group. To minimize interference of docker binding to the affinity of scFv, we placed the binding site at the C terminal of scFv where the affinity tag for purification is located. To add Sortase recognition peptides (LPETGG) and to substitute Streptag to 6xHis tag, site-directed mutagenesis was performed using NEB Q5 Site-Directed Mutagenesis Kit. The plasmid construct was transformed into B21(DE3) competent cells and transformed cells were cultured on antibiotic selective LB agarose plates at 37°C overnight. Next day, single colony was inoculated into 50 mL terrific broth (TB) medium with the antibiotics and cultured overnight in a shaking incubator at 37°C. After the overnight culture, 20 mL of culture was diluted into 1 L fresh TB medium and the culture was continued until absorbance at 600 nm (OD600) reaches to 1.5-1.8. Once OD600 reached to the point, 0.1 mM of IPTG was added to induce the expression of scFv and culture was continued at room temperature for 22-24 h. After the culture, cells were collected by centrifuging at 6000g for 15 min, the pellet was resuspended in 10 mL lysis buffer (200 mM Tris, pH 8, 20% sucrose, 1 mM EDTA, 10 mM imidazole) and incubated on ice for 30 min. Released scFv was collected by centrifuging the mixture at 20,000 g for 1 h and taking the supernatant. The supernatant was dialyzed for 48 h at 4°C with 3 times of buffer exchange with wash buffer (20 mM Tris Base, pH 7.6, 150 mM NaCl, 10 mM imidazole) to get rid of sucrose. After dialysis, His-tagged scFv was purified using Ni-NTA affinity chromatography, eluted by elution buffer (20 mM Tris Base, pH 7.6, 150 mM NaCl, 500 mM imidazole). The buffer was exchanged into storage buffer (20 mM HEPES pH 7.5, 150 mM NaCl, 10 mM CaCl<sub>2</sub>, 10% glycerol) to remove imidazole and for further reaction using Amicon centrifugal filter (10k MWCO). The concentration of scFv was measured by absorbance at 280 nm (ε<sub>scFv</sub> = 51,130 M<sup>-1</sup>cm<sup>-1</sup>). The protein was flash frozen with liquid nitrogen and stored at -80°C until further usage.

### Sortase A mediated conjugation and copper-free click chemistry of scFv-docker

To make the probe for DNA-PAINT imaging of GluA1-AMPARs, we conjugated antiGluA1-scFv and docking DNA strand via Sortase A-mediated reaction and copper-free click chemistry. 24,25 Briefly, 10-30 μM scFv with Sortase recognition peptide sequence was mixed with 130 μM Sortase A (Δ59) and 10 mM DBCO-amine in Sortase reaction buffer (20 mM HEPES pH 7.5, 150 mM NaCl, 1-10 mM CaCl<sub>2</sub>) and incubated at room temperature for 2.5-16 h on a shaker. After the reaction, unlabeled scFv and Sortase were removed by using Ni-NTA affinity chromatography. Free DBCO-amine was removed by using Amicon centrifugal filter (10k MWCO). Final concentration of DBCO labeled scFv is measured by absorbance at 280 nm and 309 nm ( $\varepsilon_{scFv} = 45,630 \text{ M}^{-1}\text{cm}^{-1}$ , ε<sub>DBCO</sub> = 12,000 M<sup>-1</sup>cm<sup>-1</sup>, CF<sub>DBCO, 280 nm</sub> = 1.07). After the first reaction, scFv-docker conjugates were made by copper-free click chemistry. Azide modified docker DNA oligo was added to DBCO-scFv with 1.5-2 times excess molecular amount and incubated at 4°C for 16-24 h. Then, free DNA oligos were removed by using Amicon centrifugal filter (30k MWCO). Final concentration of scFv-docker was measured by absorbance at 260 nm and 280 nm.

### Labeling DNA oligo with fluorophores

For making fluorophore labeled imager DNA oligo, amine-modified DNA oligonucleotides were labeled with fluorophores which have NHS ester group. Briefly, amine-modified DNA oligo was mix with 20 times excess amount of NHS ester dye in tetraborate buffer (pH 8.5). After mixing, the mixture was incubated at 4°C overnight. After the reaction, fluorophore labeled DNA oligo was purified from unreacted free fluorophore by ethanol precipitation and resuspended in molecular biology grad water. The concentration and degree of labeling of DNA oligo were calculated by Beer-Lambert equation, with the absorbance at 260 nm and at the peak absorbance of the fluorophore measured by Nanodrop spectrometer.

### Microscope setup

Imaging experiments were performed using Nikon inverted microscope (Ti-Eclipse) system. Four laser lines (MLC 400B, Agilent Technologies, equipped with 405, 488, 561, 640 nm) were combined through single mode optical fiber and focused on the back focal plane of the objective lens (APO 100x, NA 1.49, Nikon) which was used for illumination and collection of photons. Samples were loaded on xyz-translational stage (xy: motorized, z: piezo). Focus was maintained by Nikon perfect focus system (PFS). For 3D measurement a cylindrical lens (f<sub>cvl</sub> = 10 m) was put in the slide-in port between the objective lens and the tube lens to generate astigmatism.<sup>28</sup> Quad-band dichroic mirror (Chroma, ZT405-488-561-640RPC) was used for separating excitation and fluorescence emission, band pass filters were used for each spectrum (447/60, 525/50, 600/50, and 680/40). A back illuminated EMCCD camera (DU897, Andor Technology) was used for recording fluorescence signal. For drift correction, 760 nm LED was used for illuminating the sample from the top and transmitted IR signal was collected by separate IR sensitive CMOS camera (DMK 23U274, The Imaging



Source) after reflected by 750 nm long pass dichroic mirror placed above the quad-band dichroic mirror. For image acquisition and device control Nikon NIS Element and IC capture were used.

#### **Buffers**

Following buffer solutions were used in this work.

- ACSF (HEPES buffered): 20 mM HEPES pH 7.4, 125 mM NaCl, 2.5 mM KCl, 2 mM CaCl<sub>2</sub>, 1 mM MgCl<sub>2</sub>, 10 mM D-glucose
- ACSF+: ACSF +0.05% Tween 20

### **DNA-PAINT** image acquisition

For in vitro DNA-PAINT imaging, microfluidic channel was used for sample preparation. 5 / biotinylated docker was sparsely (50 p.m. concentration) immobilized on the surface of PEGylated coverslip (1-5% biotin-PEG) via streptavidin-biotin reaction. After washing free DNA strand in the solution streptavidin conjugated polystyrene beads (D = 1 μm) was added and immobilized on the surface as fiducial markers for stage drift correction. After immobilizing the beads, 0.64 nM of imager DNA was added into the channel and the apertures were sealed by vacuum grease to prevent the evaporation of imaging buffer solution during the measurement.

For live cell imaging, surface GluA1-AMPARs were labeled by 100 nM of anti-GluA1 scFv with 2.5% casein for 5 min and the cell was washed by ACSF solution 3 times. Imaging buffer solution with 1 nM imager DNA was added, and imaging was performed. For a neuron, 20 s of PALM imaging of antiHomer1-mGeos was taken with 488 nm illumination and 405 nm photoactivation pulse every 20 frames. Then 200 s of DNA-PAINT imaging of GluA1-AMPARs were taken sequentially. Camera exposure time was 100 ms.

Prepared samples were imaged on Nikon inverted microscope with 10-20 W/cm<sup>2</sup> illumination of 640 nm laser to minimize photoinduced damage of DNA probes and cells. Imaging experiments were performed at room temperature.

### scFv specificity experiments

Live neurons were incubated in HBS buffer containing 5% casein, 50 nM mouse αGluA1 antibody (Abcam, Cat# ab174785), and 100 nM scFv-Alexa 647 or 100 nM scFv-16xR1 for 5 min. Cells were then washed with HBS before fixation with 4% PFA and 4% sucrose (w/v) and washed again after fixation. They were then incubated overnight in 1000x diluted Rhodamine (TRITC)-conjugated AffiniPure F(ab')<sub>2</sub> Fragment Goat Anti-Mouse IgG (H + L) (Jackson ImmunoResearch, #115-006-062) overnight at 4°C. After washing, cells labeled with scFv-16xR1 were imaged with blocking buffer (1 mM dextran sulfate, 0.1 mg/mL sheared salmon sperm DNA, 0.05% Tween 20, 3% BSA in HBS) while cells labeled with scFv- Alexa 647 were imaged in HBS. Snapshots were taken of the TRITC signal followed by either 200 s of DNA-PAINT imaging of scFv-16xR1 or a snapshot of the scFv-Alexa 647. Exposure time was 100 ms. Diffraction limited DNA-PAINT images were created by maximum intensity projection. Whole images were then analyzed by a pixel-to-pixel comparison to calculate the Pearson's correlation coefficient.

### **QUANTIFICATION AND STATISTICAL ANALYSIS**

For analysis of image, post-processing, and data visualization, ImageJ plug-in ThunderSTORM, 44 Picasso DNA-PAINT analysis software package, and custom codes written in MATLAB or Python 3 were used. Statistical results are represented mean ± SE of mean or SD as mentioned in each figure. Details for each step are described in following subsections.

### Single molecule localization

For single molecule localization, single molecules were detected by using either ImageJ plugin ThunderSTORM with B-spline filter 44 and peak intensity threshold (2\*std(Wave.F1)), or Picasso DNA-PAINT analysis software package with gradient-based method were used. Detected fluorescent signals were fitted with a 2D Gaussian function via MLE to estimate the molecule's position, signal photons, background photons and the width of the PSF. For 2D imaging symmetric Gaussian model was used and for 3D astigmatism elliptical Gaussian model was used with calibration.<sup>28</sup> Stage drift was corrected as done in the previous literature.<sup>45,46</sup> Briefly, polystyrene beads immobilized on the glass surface were imaged by IR sensitive CMOS camera, and the position of the beads was subtracted from the position of detected fluorescent molecules according to the frame.

### Calculation of kon and koff of imager to the surface immobilized docker in vitro

To calculate kon and koff of imager-docker pairs, a single docker was picked using Render module of Picasso package. Specific binding of imager to the docker visualized sparsely located docker strands showing confined clusters in the reconstructed image (Figure S2). From an individual docker, the on-time and off-time of bindings were obtained by calculating the mean of the duration of binding (on-time) and the interval between two adjacent binding (off-time) using Render module of Picasso package.

### Diffusion coefficient and trajectory range

For tracking of single particle Crocker-Grier algorithm was used. 47 Briefly, the localization information (x,y,z-position and time) and three input parameters are given, including maximum displacement of particle between adjacent frames (500 nm), minimum length of trajectory in frame (5 frames) and maximum dark time to compensate blinking of the dye or missing signal due to noise (3 frames). The



algorithm links the localizations molecules showing up within maximum displacement and maximum dark time to detect the trajectories of the molecules. After the linkage, the trajectories shorter than minimum length were eliminated to filter out noise. The mean squared displacement (MSD, Figure S12) curve of the trajectories ( $\langle x^2 \rangle$ ) were fitted with linear curve and the diffusion coefficient D was calculated based on following equation.

$$D = \frac{\langle x^2 \rangle}{2nt}$$

where n is the dimension of the trajectory and t is the time. Trajectory range is calculated by taking maximum distance between localizations within a trajectory.

For the visualization of the data, density scatterplot of the diffusion coefficient and the range of individual trajectory was shown in 2D plane in logarithmic scale. For quantification of mobile and immobile trajectories, Gaussian Mixture Model (function "fitgmdist") was used to fit the data with two 2-dimensional Gaussian functions (number of components, k = 2) using custom MATLAB code. Based on the axial localization accuracy, which is poorer than the lateral accuracy of the image ( $\sigma_z = 75$  nm), we defined the limit of detection of diffusion coefficient and trajectory range (D<sub>LOD</sub> and Traj<sub>LOD</sub>, respectively) calculated by the equations below as immobile group.

$$D_{LOD} = \frac{\langle \sigma_z \rangle^2}{6t} = 10^{-2.5} (= 0.003) \mu m^2 / s$$

$$Traj_{LOD} = 2.355\sigma_z = 10^{-0.75} (= 0.178) \ \mu m \ for \ \sigma_z = 75 \ nm$$

The distribution showing the diffusion coefficient and trajectory range below the LOD were determined immobile.

### **Nanodomains**

Nanodomains of GluA1-AMPARs were defined by the cluster of immobile (D <  $10^{-2.5} \mu m/s^2$ ) GluA1-AMPAR localization in synaptic regions. To measure the size of the nanodomains, x, y, z positions of the localizations were fit with 3-dimensional Gaussian function and the  $\sigma_x$ ,  $\sigma_y$ , and  $\sigma_z$  were obtained as the length of three axis. The volumes were calculated by

$$V = \frac{4}{3}\pi\sigma_x\sigma_y\sigma_z$$